# Nanocomposites Containing Silica-Coated Gold–Silver Nanocages and Yb–2,4-Dimethoxyhematoporphyrin: Multifunctional Capability of IR-Luminescence Detection, Photosensitization, and Photothermolysis

**Boris Khlebtsov,[†] Elizaveta Panfilova,[†] Vitaly Khanadeev,[†] Olga Bibikova,[†] Georgy Terentyuk,[‡] Andrey Ivanov,[§] Valentina Rumyantseva,[⊥] Igor Shilov,[¶] Anastasia Ryabova,[#] Victor Loshchenov,[#] and Nikolai G. Khlebtsov[†,‡,*]**

[†]Institute of Biochemistry and Physiology of Plants and Microorganisms, Russian Academy of Sciences, 13 Prospekt Entuziastov, Saratov 410049, Russia, [‡]Saratov State University, 83 Ulitsa Astrakhanskaya, Saratov 410012, Russia, [§]Blokhin Russian Cancer Research Center, Russian Academy of Medical Sciences, 24 Kashirskoe Shosse, Moscow 115478, Russia, [⊥]Lomonosov Moscow State Academy of Fine Chemical Technology, 86 Prospekt Vernadskogo, Moscow 119571, Russia, [¶]Kotelnikov Institute of Radio Engineering and Electronics (Fryazino Branch), Russian Academy of Sciences, 1 Ploshchad Vvedenskogo, Fryazino 141190, Moscow Region, Russia, and [#]Natural Sciences Center, Prokhorov General Physics Institute, Russian Academy of Sciences, 38 Ulitsa Vavilova, Moscow 119991, Russia

**ABSTRACT** We describe novel composite nanoparticles consisting of a gold–silver nanocage core and a mesoporous silica shell functionalized with the photodynamic sensitizer Yb–2,4-dimethoxyhematoporphyrin (Yb–HP). In addition to the long-wavelength plasmon resonance near 750–800 nm, the composite particles exhibited a 400-nm absorbance peak and two fluorescence peaks, near 580 and 630 nm, corresponding to bound Yb–HP. The fabricated nanocomposites generated singlet oxygen under 630-nm excitation and produced heat under laser irradiation at the plasmon resonance wavelength (750–800 nm). In particular, we observed enhanced killing of HeLa cells incubated with nanocomposites and irradiated by 630-nm light. Furthermore, an additional advantage of fabricated conjugates was an IR-luminescence band (900–1060 nm), originating from $Yb^{3+}$ ions of bound Yb–HP and located in the long-wavelength part of the tissue transparency window. This modality was used to control the accumulation and biodistribution of composite particles in mice bearing Ehrlich carcinoma tumors in a comparative study with intravenously injected free Yb–HP molecules. Thus, these multifunctional nanocomposites seem an attractive theranostic platform for simultaneous IR-luminescence diagnostic and photodynamic therapy owing to Yb–HP and for plasmonic photothermal therapy owing to Au–Ag nanocages.

**KEYWORDS:** plasmonic nanoparticles · nanocomposites · photodynamic therapy · hematoporphyrin · theranostics · HeLa cells · xenografted mouse tumor model

Photodynamic therapy (PDT) of oncological diseases[1,2] and some dermic and infectious diseases is based on selective accumulation of photosensitizers (PSs) followed by light irradiation at an appropriate wavelength.[3] Type II PSs used in PDT are nontoxic in the dark, but when exposed to light, they begin to generate reactive oxygen species such as singlet oxygen and free radicals. These reactive oxygen species cause oxidization of cancer cell components and their irreversible damage.

To date, several classes of PSs have been approved or are under preclinical testing for PDT. These include porphyrins, chlorines and bacteriochlorins, phthalocyanines, phenothiazinium compounds, texafrins, *etc.*[4] Their spectral maxima of singlet-oxygen generation are located in the red or NIR band, from 630 nm (porphyrins) to 730–780 nm (texafrins and bacteriochlorins),[3,5] and their absorption coefficients vary from 10000 $cm^{-1}$ $M^{-1}$ (porphyrins) to 170000 $cm^{-1}$ $M^{-1}$ (phthalocyanines).[6] Although the fluorescence maxima of most PSs lie in the visible spectral band, some metallocomplexes of PSs (for instance, Yb–hematoporphyrins[7]), exhibit additional luminescence bands in the NIR region. This additional modality is important for diagnostic purposes *in vivo*, as the known tissue transparency window is located within 700–1000 nm.[8]

Despite the long scientific story, the current PDT technologies and PS delivery systems are not free from serious drawbacks.

Received for review May 17, 2011 and accepted August 14, 2011.

**Published online August 15, 2011**
10.1021/nn2017974

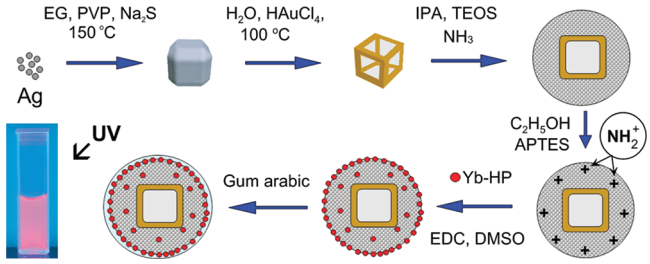


**Figure 1. Schematic illustration summarizing how fluorescent composite nanoparticles can be fabricated starting with Ag nanocubes and ending with silica-coated Au–Ag nanocages functionalized with Yb–HP molecules. The left-bottom photo shows visible fluorescence of a sample under UV excitation. Designations: EG, ethylene glycol; PVP, poly(vinyl pyrrolidone); IPA, isopropyl alcohol; TEOS, tetraethyl orthosilicate; APTES, 3-aminopropyltriethoxysilane; Yb–HP, Yb–2,4-dimethoxyhematoporphyrin; EDC, 1-ethyl-3-(3-dimethylaminopropyl) carbodiimide; DMSO, dimethyl sulfoxide.**

Most photosensitizers are hydrophobic species and can aggregate after intravenous injection. Accordingly, the administered dose should be increased in order to maintain PDT efficiency, thus causing potential toxicity to healthy tissues. For circumventing these drawbacks, significant efforts have been devoted to loading PSs into various colloidal carriers[9] that protect PSs from aggregation in a physiological environment and ensure their homogeneous distribution in target tissues. In the past few years, several types of nanoparticles have been examined as potential PS carriers.[3,10] Such nanoparticles can be optically active PDT moieties (for instance, quantum dots,[11] porphyrin nanoparticles,[12] self-illuminating nanoparticles,[13] *etc.*) or can be used as passive carriers for targeted PS delivery. For example, PS-loaded liposomes and micelles can enhance tumor uptake and increase cytotoxicity to tumor tissues, as compared to free PSs.[14,15] Moreover, wavelength selective light-induced release from gold-coated liposomes has been reported recently,[16] thus making PS delivery to be light-controlled in principle.

One of the most popular PS carriers are mesoporous silica nanoparticles, which have already been employed as delivery systems for several applications,[17] including delivery of doped porphyrins.[18,19] The major advantages of silica nanoparticles is their high pore volume and large surface area, making doped PS a more efficient and nonaggregated producer of singlet oxygen. Moreover, silica-based nanostructures have good biocompatibility and can easily be functionalized with various probe molecules. All these properties make mesoporous silica very attractive for PDT applications.

A new trend in current nanobiotechnology and theranostics is the fabrication of multifunctional nanoparticles, which combine the therapeutic and diagnostic modalities in a single nanostructure.[20,21] From this point of view, an attractive option is nanostructures combining the unique optical properties of plasmonic nanoparticles[22] with the advantages of mesoporous silica functionalized with appropriate PSs.[20] However, the available data on such composites are very limited at present. In particular, there are only few publications describing conjugates of colloidal gold nanoparticles with porphyrins[23–28] and phthalocyanine.[29,30] Recently, Zhao *et al.*[31] reported the first fabrication of nanocomposites comprising a gold nanorod core and a mesoporous silica shell doped with hematoporphyrin (HP). The authors demonstrated more efficient generation of singlet oxygen by composites, as compared to free HP, and multifunctional properties through two-photon bioimaging of cells treated with nanocomposites.

In this work, we describe a novel type of nanocomposite based on silica-coated gold–silver nanocages functionalized with the photodynamic sensitizer Yb–2,4-dimethoxyhematoporphyrin (Yb–HP). The fabricated nanoparticles combine several promising theranostic modalities: (i) an easy tunable plasmon resonance across the 650–950-nm spectral band with possible use as plasmonic heating labels;[32,33] (ii) a mesoporous silica shell that preserves the plasmon resonance from an aggregation shift[34] and provides a convenient possibility of surface or volume functionalization with various molecular probes;[17,35] (iii) a combination of singlet oxygen generation with an additional, 900–1060-nm IR-luminescence band of Yb–HP,[7,36] which can be used for optically controlled PDT within the tissue transparency window.

## RESULTS AND DISCUSSION

**Fabrication and Characterization of Nanocomposites.** A general scheme for the synthesis of composite nanoparticles includes three basic steps (Figure 1). At the first step, silver nanocubes are prepared by the sulfide-mediated polyol method[37] (with minor modifications[33]), in which Ag(I) is reduced to Ag(0) with ethylene glycol in the presence of poly(vinyl pyrrolidone) (PVP), and ethylene glycol serves both as a solvent and as a reducing agent. It should be emphasized that the preparation of high-quality Ag nanocubes is a crucial step in Au–Ag nanocage fabrication by the galvanic replacement reaction.[37] According to the method described in ref 37, a trace amount of $Na_2S$ is added to the reaction mixture in order to limit the formation of twinned Ag seeds and to promote Ag cube formation. Besides, in this reaction, PVP selectively binds to {100} Ag facets to facilitate further the formation of a cubic shape. The average Ag cube size can be controlled within the 30–60 nm range by

varying the reaction conditions.[37,38] After fabrication of Ag cubes, they serve as templates for a galvanic replacement reaction between Ag and $HAuCl_4$ and for the formation of a partly hollow Au–Ag alloyed nanostructures called nanocages.[37,39] This reaction involves the addition of an aqueous $HAuCl_4$ solution to a boiled suspension of Ag nanocubes. The spectral shift of the plasmon resonance from 435 nm to 650–900 nm can be tuned only by controllable addition of $HAuCl_4$, and the reaction can be stopped at any point to fabricate Au–Ag nanocages with a desired particle structure and plasmon resonance wavelength.

At the second step, a mesoporous silica shell around a nanocage core is fabricated *via* base-catalyzed hydrolysis of tetraethyl orthosilicate (TEOS),[40] as described in Methods. Specifically, the silica shell was grown by reducing TEOS with $NH_4OH$ in the presence of isopropyl alcohol. The silica shell thickness can be controlled over the 20–120 nm range by varying the TEOS concentration and the reaction time.

The final, third, step involves the amination of silica with amine groups by a reaction with 3-aminopropyltriethoxysilane (APTES) followed by functionalization of nanocomposites with Yb–HP and the stabilization of nanocomposites by gum arabic to make them biocompatible. Note that by contrast to amination of silica nanospheres in gold-nanoshell fabrication,[41] the electrostatic interaction between Yb–HP and $NH_2^+$ amine groups is used here at the initial stage of functionalization followed by chemical cross-linking through 1-ethyl-3-(3-dimethylaminopropyl) carbodiimide (EDC).

Figure 2 shows TEM images and photos of cuvettes with Ag nanocubes, Au–Ag nanocages, and silica-coated nanocages (Figure 2 panels a,b,c, respectively). From the TEM data [see Supporting Information (SI), Figure S1], the average edge of silver cubes equals $L_{av}$ = 40.5 ± 5 nm and the average yield is about 90%. Along with these cubes, the TEM images also reveal the minor presence of triangle and rodlike particles (SI, Figure S1). For high-quality cubes, the extinction spectrum demonstrates a sharp major plasmon resonance near 435 nm and two additional resonances at 354 and 391 nm (Figure 2d, curve 1). Actually, the second resonance looks like a weak shoulder because of the small size of the Ag cubes. For larger cubes, the second resonance can be clearly seen.[37,38]

The replacement reaction between Ag and $HAuCl_4$ results in the formation of nanoboxes, nanocages (Figure 2b, insets), and other porous particles of the nanocage family with the average particle size $L_{av}$ = 46.4 ± 5 nm (Figure 2b and SI, Figure S2). According to the TEM data, the average thickness of the nanobox wall is about 5–6 nm. The transformation of Ag cubes into nanocages is accompanied by shifting of plasmon resonances of extinction[37] and static light scattering[33] from the blue to the 700–900 nm NIR band, depending

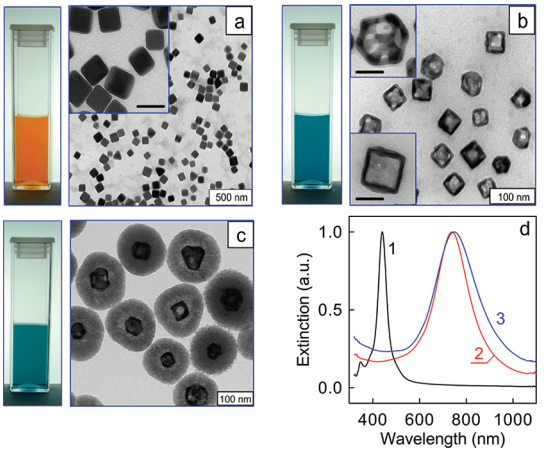


**Figure 2. TEM images and photos of samples with silver nanocubes (a), Au–Ag nanocages (b), and composite silica-coated nanocages (c). The insets in panel b illustrate the box and cage particle morphologies. Panel d shows the extinction spectra for Ag cubes (1), Au–Ag nanocages (2), and composite Au–Ag/$SiO_2$ particles (3). The scale bars in the insets are 50 nm.**

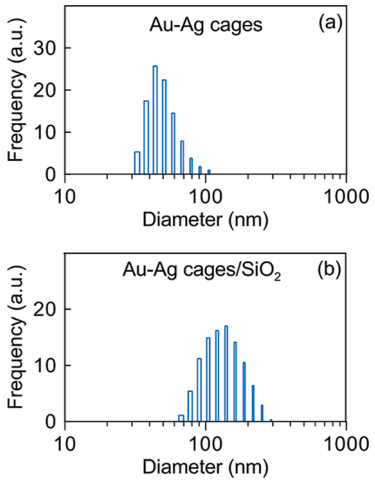


**Figure 3. DLS number–size particle distributions of Au–Ag nanocages (a) and silica-coated Au–Ag nanocages (b). The number-averaged DLS diameters of Au–Ag and Au–Ag/$SiO_2$ particles are 50.8 ± 5 nm and 140.4 ± 14 nm, respectively, and the average DLS thickness of the silica shell is about 45 nm.**

on the particle size and structure (Figure 2d, curve 2). As the complete stoichiometric conversion of Ag to Au results in nanocage fragmentation, the replacement reaction was stopped when the extinction spectrum was moved to a desired wavelength (750 nm for spectrum 2). Thus, our nanocages still contain some percentage of Ag (about 30–40%, according to the atomic absorption spectroscopy data).

The prepared Ag nanocubes and Au–Ag nanocages exhibit good monodispersity according to the TEM data. Specifically, the relative full-width half-maximum of the number-size distributions of Ag nanocubes and Au–Ag nanocages is 12% and 10%, respectively.

The TEM images of composite nanoparticles are shown in Figure 2c and Figure S3 (SI). They demonstrate quite homogeneous and uniform silica shells of 40- and 45-nm thickness, as determined from TEM and dynamic light scattering (DLS) data, respectively (Figure 3). As the intrinsic formation mechanism of the Stöber method is the coalescence of small silica nanospheres, the mesoporous structure of silica shells (similar to the previously reported observations[31,42]) can be seen in enlarged TEM images (SI, Figure S3). As pointed out by Zhao *et al.*,[31] such a mesoporous structure can enhance the generation of singlet oxygen and can facilitate its release from doped porphyrin molecules to the surrounding medium. Compared with Au–Ag nanocages, the longitudinal plasmon band of silica-coated Au–Ag/$SiO_2$ is slightly red-shifted, which is similar to the known effects of external dielectric coating around plasmonic nanoparticles.[22]

Functionalization of composite nanoparticles with porphyrins can be performed by a two-step method described in ref 31, in which a thin silica layer is deposited first and then the second layer is created by coating Au/$SiO_2$ nanoparticles with hematoporphyrin-functionalized silanization precursors. Here, we used a one-step cross-linking protocol that involves amination of silica with amine groups by a reaction with APTES followed by chemical cross-linking through EDC (see Methods). Figure 4 shows the extinction spectra of silica-coated nanocages (Au–Ag/$SiO_2$) and composite nanoparticles functionalized with Yb–HP molecules (Au–Ag/$SiO_2$/Yb–HP nanoparticles). For comparison, the spectrum of a free Yb–HP solution with a characteristic absorption maximum near 400 nm is also plotted on the same graph. Along with the 790-nm plasmon resonance peak, the spectrum (3) reveals an additional, 400-nm maximum located just at the major absorption peak of Yb–HP. This observation confirms that Yb–HP molecules have been successfully attached to the composite nanoparticle surface *via* the one-step functionalization protocol.

To roughly estimate the number of Yb–HP molecules bound to one composite particle, we applied the following approach. First, we used a calibration curve (SI, Figure S4) to find that the Yb–HP concentration was about 20 mg/L in a free Yb–HP solution (Figure 4, spectrum 1). Almost the same concentration was found for functionalized composite nanoparticles, as the 400-nm maxima for composites (Figure 4, curve 3) and superposition of spectra 1 and 2 (Figure 4, curve 4) coincided. The numerical concentration of nanocages was estimated by two methods. First, we used the initial mass of silver (50 mg) distributed over 41-nm silver cubes in a 40 mL volume to find the number concentration $N_{Ag} = 2.1 \times 10^{15}$ cubes/L. Then, keeping in mind all preparative manipulations, we found $N = 2 \times 10^{14}$ Au–Ag cages/L.

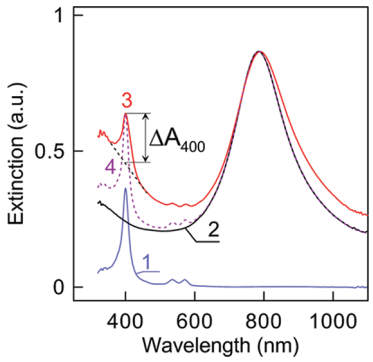


**Figure 4. Extinction spectra of free Yb–HP solution (curve 1, concentration of about 20 mg/L), Au–Ag/$SiO_2$ composites (curve 2, number concentration of about $2 \times 10^{14}$ particles/L), and those functionalized with Yb–HP (3). Spectrum 4 is the superposition of spectra (1) and (2); $\Delta A_{400}$ is the difference between the nanocomposite absorption and the background absorption at 400 nm (see text). All experimental spectra were measured in a 2-mm cuvette.**

In the second method, we used the experimental extinction $A_{max} \cong 0.9$ (Figures 2 and 4), the optical path $l = 0.2$ cm, and the experimental extinction cross section $\sigma_{ext} \cong 7 \times 10^{-15}$ m$^2$ for 45-nm Au–Ag nanocages.[43] Then, calculations by the known single-scattering and absorption formula[44] $N_p = 2.3A_{max}/(\sigma_{ext}l)$ gave $1.5 \times 10^{14}$ particles/L, in reasonable agreement with the above mass–volume estimate of $2 \times 10^{14}$ particles/L. Finally, we used the molecular mass of Yb–HP (873 Da[7]) to find the number of bound molecules per composite particle, $N_{HP}/N_p \cong 7 \times 10^4$.

This crude calculation seems overestimated because of the overvalued concentration of bound Yb–HP, which was found from absorption $A_{400}$. However, it would perhaps be more correct to calculate the concentration of bound Yb–HP from the difference between the nanocomposite absorption and the background absorption at 400 nm, $\Delta A_{400} \cong 0.2$ (Figure 4), which corresponds to a Yb–HP concentration of about 10 mg/L. Then, by dividing the plasmon resonance extinction $A_{max} = 0.434\sigma_{ext}N_pl$ and the contribution of Yb–HP to the absorption at 400 nm $\Delta A_{400} = 0.434\varepsilon_{400}[c]l$ ([$c$] is the molar concentration of bound Yb–HP), we get the following equation:

$$\frac{N_{HP}}{N_p} = \frac{\Delta A_{400}}{A_{max}} \frac{\sigma_{ext}N_A}{\varepsilon_{400}} \qquad (1)$$

where $\varepsilon_{400}$ is the molar absorption coefficient (cm$^{-1}$ M$^{-1}$) and $N_A$ is the Avogadro number. After introducing $\sigma_{ext} \cong 7 \times 10^{-15}$ m$^2$, $\Delta A_{400}/A_{max} \cong 0.23$, and $\varepsilon_{400} = 2 \times 10^5$ cm$^{-1}$ M$^{-1}$ into eq 1, we get $N_{HP}/N_p = 4.8 \times 10^4$.

It is instructive to compare our $N_{HP}/N_p$ ratios with those reported by Zhao *et al.*[31] from the absorption spectra of gold-nanorod–HP composites. From their data, $A_{725} = 0.34$ and $[c_{HP}] = 5.6 \times 10^{-8}$ M, we find $A_{400}/A_{725} = 0.14$. By using an experimental estimate of the extinction coefficient for rods $\sigma_{ext} \cong 1 \times 10^{-15}$ m$^2$,[43] we get $N_{HP}/N_p = 4200$, which is almost two times greater

than the reported value of 1900.[31] However, both numbers (4200 and 1900) are significantly lower than the above estimate of $4.8 \times 10^4$ for our nanocomposites. This difference, at least partly, can be attributed to the difference in the particle surface area. Indeed, the ratio between the surface areas for silica-coated nanocages (120 nm in diameter) and nanorods ($15 \times 45$ nm)[31] is about 6, which is almost two times lower than $4.8 \times 10^4/4.2 \times 10^3 = 11.4$. Therefore, the above high load of the fabricated nanocomposites with Yb–HP ($4.8 \times 10^4$ molecules per particle) means some type of volume or aggregate distribution within the silica shell, rather than monolayer packing.

For possible applications, it is important to demonstrate the integrity of fabricated hybrid nanoparticles to variations in pH, washing, and potential leaching of the dye molecules. The integrity test was performed by changing the pH of nanocomposite solutions from 2 to 13, which was followed by centrifugation, redispersion of particles, and spectroscopic examination of the redispersed samples at the same pH (see Methods). Figure 5a shows extinction spectra of three redispersed samples with pH 2, 7, and 13. Because of possible particle aggregation at low and high pH, the spectra reveal slight variations near the plasmonic peak and in the short-wavelength region below 600 nm. However, the Yb–HP peaks at 400 nm are clearly seen in all three spectra. This confirms the integrity of our nanocomposites at low, medium, and high pH after centrifugation and washing. To make this conclusion more convincing, we plotted the short-wavelength parts of the spectra in Figure 5b and extracted the Yb–HP absorption peaks by subtraction of the backgrounds (dashed lines in Figure 5b) from the extinction spectra. The resultant Yb–HP peaks of redispersed nanocomposites at pH 2, 7, and 13 (Figure 5c) are almost the same within the limits of experimental error. Similar results were obtained for a longer incubation time (10 h; see SI, Figure S4c and S4d).

For normalization of experimental data [*e.g.*, for the deoxygenation of blood samples with fabricated nanocomposites (see later)], one needs to accurately quantify Yb–HP in composite particles in order to account for the variation in dye loading between each batch of particles. Although the spectra of free Yb–HP and those within the particles are similar, it would be desirable to have a direct technique for determination of Yb–HP content in hybrid particles. To this end, we used a method in which washing of the Yb–HP molecules out of the composites was followed by spectroscopic examination (see Methods). We found that the Yb–HP molecules could be washed out of the composites by a mixture of ethanol (45%, v/v), dimethyl sulfoxide (DMSO, 45%), and water (10%).

In Figure 6, we compare two methods for quantifying Yb–HP in nanocomposites with a 60-nm silica shell. The first method was explained in Figure 4 and

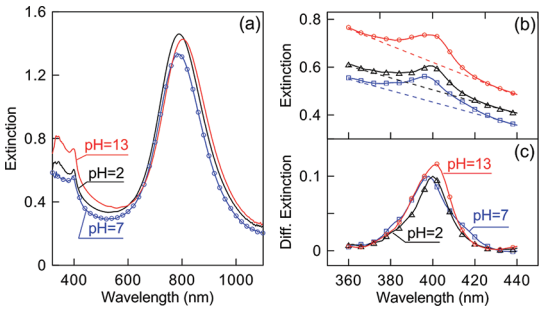


**Figure 5. (a) Extinction spectra of nanocomposite solutions at pH 2, 7, and 13 after incubation (10 min), centrifugation, and redispersion. For comparison, the circles show the initial spectrum before pH adjustment and centrifugation–redispersion. Panels b and c show the short-wavelength parts of the spectra (b) and the Yb–HP absorption peaks (c) obtained by subtraction of the background (dashed lines).**

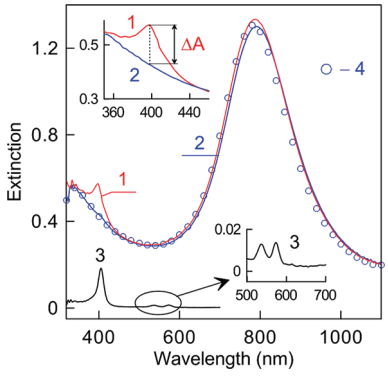


**Figure 6. Extinction spectra of composite particles in water before (1) and after (2) washing off the Yb–HP molecules. Curve 3 shows an absorption spectrum of Yb–HP molecules in the washing ethanol–DMSO–water mixture (see Methods). For comparison, the circles (4) show an extinction spectrum of silica-coated nanocages before functionalization with Yb–HP molecules (Au–Ag/$SiO_2$, silica shell thickness of about 60 nm). The left-top inset illustrates determination of Yb–HP from the difference ($\Delta A$) between the extinctions of nanocomposites and silica-coated nanocages. The right-bottom inset shows an enlarged fragment with two additional characteristic peaks of Yb–HP at 536 and 573 nm. All spectra were measured in a 2-mm cuvette.**

utilizes the difference $\Delta A$ between the extinctions of nanocomposites and silica-coated nanocages. From the left-top inset in Figure 6, $\Delta A = 0.142$, and from water calibration of SI, Figure S4a, we obtain a Yb–HP concentration of 7.4 mg/L, which is somewhat lower than the above estimate (10 mg/L) for the sample in Figure 4 with a 40-nm silica shell. The second method is based on the above-described washing technique. Figure 6 shows extinction spectra of composites before (1) and after (2) washing off the Yb–HP molecules and an absorption spectrum of the washed-off molecules in ethanol–DMSO–water. The absorption peak $A_{400} = 0.183$ and the calibration curve in SI, Figure S4b (ethanol–DMSO–water was used as a solvent for free Yb–HP) yield a Yb–HP concentration of 7.1 mg/L, in

good agreement with the above estimate of 7.4 mg/L for nanocomposites. Thus, both methods give consistent data for the Yb–HP molecules included in the hybrid particles.

**Luminescent and Photodynamic Properties of Nanocomposites.** It is well-known[45] that the energy transfer process from fluorescent molecules to metal nanoparticles results in emission quenching and can reduce singlet oxygen generation efficiency. However, in the nanocomposites prepared by our one-step method, the mesoporous silica layer prevents direct contact between Yb–HP molecules and nanocages, thus preventing energy transfer from Yb–HP to the Au–Ag core. Extensive measurements of the luminescence emission spectra at 400-nm excitation with a broad range of nanocomposite particle concentrations ($2 \times 10^{14}$ to $0.32 \times 10^{12}$ particles/L) and concentrations of free Yb–HP (20 mg/L to 32 $\mu$g/L) revealed nonlinear behavior of the spectra (SI, Figure S5) except for the dilute samples discussed below.

Figure 7 shows typical fluorescent emission spectra recorded at a 400-nm excitation of free Yb–HP and Au–Ag/$SiO_2$/Yb–HP water solutions at roughly equivalent concentrations of Yb–HP (32 $\mu$g/L). Two fluorescence peaks at 580 and 630 nm and a weak fluorescence band near 680 nm are clearly seen for both Yb–HP and nanocomposite solutions. Two fluorescence bands near 620–630 and 670–680 nm are well-known for free HP molecules. However, to the best of our knowledge, the intense 580-nm emission peak of Yb–HP has never been reported.

From emission measurements of samples with different concentrations (SI, Figure S5), the fluorescence intensity of Yb–HP was found to be quenched with a quenching factor of about 0.7 for the most diluted sample shown in Figure 7. As the Yb–HP molecules are well separated by a 40-nm shell from the Au–Ag core, the energy transfer from Yb–HP to the metal core seems low in our nanocomposites. Perhaps an additional quenching factor is due to the large surface density of the Yb–HP molecules attached to the composite surface.

It should be emphasized that the observed fluorescence quenching in Figure 7a is quite small, about 30%. This is in contrast with the previously reported data for silica-coated gold nanorods functionalized with HP[31] (the quenching factor was about 3). We also note (SI, Figure S5) that the shape of the composite 630-nm emission band was somewhat different from that of free Yb–HP at Yb–HP concentrations above 32 $\mu$g/L.

To check whether this change in observed fluorescence spectra may have been caused by the inner filter effects (nonlinear absorption of both excitation and emission light),[46] we compared the measured and corrected spectra by using eq S1 (SI, section S3). It follows from SI, Figure S5 that the distortion of the 630-nm emission band is not related to selective attenuation of the emitted light, at least for diluted

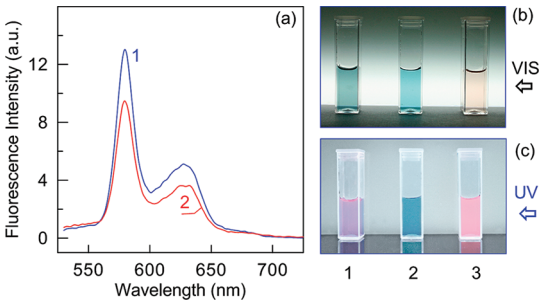


**Figure 7. (a) Fluorescence spectra of free Yb–HP (1) and composite nanoparticles Au–Ag/$SiO_2$/Yb–HP (2) at a 400-nm excitation. The concentration of Yb–HP in both samples is about 32 $\mu$g/L, and the nanocomposite concentration equals $0.32 \times 10^{12}$ particles/L. The photos on the right panel show cuvettes with the fluorescent nanocomposites Au–Ag/$SiO_2$/Yb–HP (1), silica-coated particles Au–Ag/$SiO_2$ (2), and free Yb–HP solution (3). Photos were taken under white (b) and UV (c) light excitation.**

samples. However, we cannot exclude some contribution from spurious light scattering, which could have distorted the emission spectra. Second, eq S1 only gives an approximate correction, as it does not take into account the instrumental geometry of the incident beam and the detector viewing angle (SI, section S3). Finally, the change in the 630-nm emission band could have been caused by the locally high concentration of Yb–HP molecules in (or on) the silica shell.

Straightforward evidence for the successful functionalization of composite particles with Yb–HP is provided by the photo in the right part of Figure 7. Shown here are cuvettes containing composite particles with attached Yb–HP (1), without Yb–HP (2), and with free Yb–HP molecules (3). Under white light illumination, the first two cuvettes (1 and 2) demonstrate a blue-green color and the third cuvette shows a faintish pink color because of the selective absorption near 400 nm. When irradiated with a UV lamp, the first and third cuvettes exhibit intense pink fluorescent emission, whereas the second cuvette retains its blue color.

Additional evidence for the successful functionalization of nanocomposites comes from measurements of singlet oxygen ($^1O_2$) generation. To assess the efficiency of $^1O_2$ generation in a biological environment, we applied a method developed by Stratonnikov *et al.*[47] In this method, the time-dependent consumption of oxygen in PS-containing blood samples is measured under irradiation with a low level of laser fluence when the following relationship holds:

$$\Gamma_{PDT} = f_{PDT}^{-1}[C_0]P \qquad (2)$$

where $\Gamma_{PDT}$ is the oxygen consumption rate owing to PDT (M/s), $f_{PDT}$ is the molecular oxygen consumption fluence (J/cm$^2$), $[C_0]$ is the initial molar concentration of PS, and $P$ (W/cm$^2$) is the energy fluence rate. At the initial time of irradiation, when the decrease in the PS concentration owing to photodecomposition is small, the oxygen consumption rate owing to PDT, $\Gamma_{PDT}$ (M/s)

can be calculated by the initial slope through the following equation:

$$\Gamma_{PDT} = -4[HbT]\frac{dS_{O_2}}{dt} \quad (3)$$

where $[HbT]=([Hb_1]+[Hb_1O_2])/4$ is the total molar concentration of hemoglobin in blood, $[Hb_1]$ and $[Hb_1O_2]$ are the molar concentrations of hemoglobin structural units free from oxygen and bound to oxygen molecules, respectively; and $S_{O_2} = [Hb_1O_2]/([Hb_1] + [Hb_1O_2])$ is the hemoglobin oxygen saturation. Combining eqs 2 and 3, we get

$$f_{PDT} = \frac{-4[HbT]\frac{dS_{O_2}(0)}{dt}}{[C_0]P} \quad (4)$$

where the $f_{PDT}$ parameter has the physical meaning of delivered fluence, at which for every PS molecule, one oxygen molecule is consumed in the PDT reaction. In other words, the $f_{PDT}$ parameter is equal to the number of the singlet oxygen molecules produced by one PS molecule at an irradiation dose of 1 J/cm$^2$.

Figure 8a shows the time-dependent deoxygenation of blood samples incubated with Au−Ag/$SiO_2$/Yb−HP nanocomposites (curve 2). The capability of free Yb−HP molecules and a simple mixture of Yb−HP and silica-coated Au−Ag/$SiO_2$ nanocages to generate singlet oxygen was also recorded under the same conditions for direct comparison (curves 1 and 3, respectively). The inset illustrates a typical run to follow the deoxygenation dynamics of a blood sample incubated with free HP molecules in the pulsed mode of laser irradiation with 6-s light intervals (633 nm, 30 mW/cm$^2$) followed by 10-s dark intervals. As can be seen in Figure 8a, oxygen saturation gradually decreased with increasing illumination time. From the initials slope of these curves, we calculated the PDT efficiency in terms of the $f_{PDT}$ parameter, as shown in Figure 8b. It follows from Figures 7 and 8b that both fluorescence and PDT efficiencies of Au−Ag/$SiO_2$/Yb−HP nanocomposites are slightly lower than those for the free Yb−HP molecules. The lowest PDT efficiency was recorded for a simple mixture of Yb−HP and silica-coated particles. A weak reduction in the photooxidation efficiency of nanocomposites, compared to that of free Yb−HP at the same concentration, differs from the usual strong fluorescence and PDT quenching of PSs near the metal particle surfaces.[45,48]

On the other hand, HP molecules revealed an almost three times higher PDT efficiency as compared with both free Yb−HP molecules and nanocomposites. This is not surprising, as the phototoxicity of Yb−HP metallocomplexes has been shown[7] to be relatively low because of the reduced generation of the singlet oxygen. The reason is that the $Yb^{3+}$ ion luminescence level lies between the triplet energy level of HP and the singlet oxygen level. Accordingly, the photoexcitation

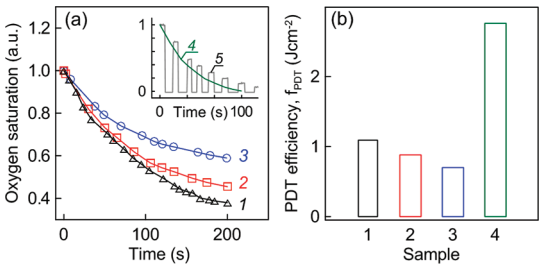


**Figure 8. (a) Oxygen saturation dynamics in three blood samples incubated with free Yb−HP (1), Au−Ag/$SiO_2$/Yb−HP nanocomposites (2), and a mixture of Yb−HP and silica-coated nanocages (3). The inset shows a typical deoxygenation record for free HP molecules (4) irradiated with 6-s light pulses (633 nm, 30 mW/cm$^2$) followed by 10-s dark pauses (5). (b) Comparison of PDT efficiency in terms of the $f_{PDT}$ parameter for the same samples 1−4 in panel a.**

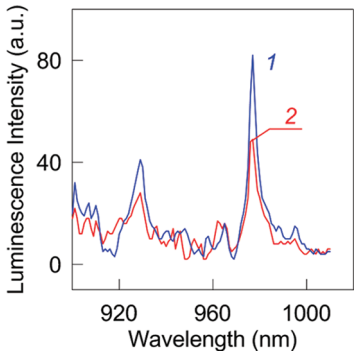


**Figure 9. NIR luminescence spectrum of free Yb−HP (1) and nanocomposites (2) in water.**

energy of HP molecules is transferred to the $Yb^{3+}$ ion rather than to oxygen, thus causing a decreased efficiency of singlet-oxygen generation. In a sense, it is a penalty for the additional IR luminescence (Figure 9) related to the transition of the 4*f* electrons of $Yb^{3+}$ ions ($^2F_{5/2} \rightarrow {}^2F_{7/2}$) owing to the excitation of $\pi$-electrons belonging to the organic part of the Yb−HP complexes.[36] Both free Yb−HP molecules in water and those included in hybrid nanoparticles reveal two IR-luminescence bands located near 930 and 977 nm. Although this IR luminescence in water is relatively weak, its spectral position can be important for potential diagnostics *in vivo* because of the low tissue absorption in this spectral band.[8]

**Photothermal and Biodistribution Properties.** Incorporating a metal-nanoparticle core into nanocomposites provides an additional important property that can be used in two modalities. First, such nanocomposites can serve as simple photothermal labels for plasmonic photothermal therapy (PPTT) of cancer[49] or as combined labels for a dual PPTT/PDT cancer therapy.[48] Further, moderate hyperthermia has been shown to release the bound anticancer drug[50] or PS,[48] which then regained its fluorescence and singlet oxygen generation, which had been quenched because of the proximity of the metal core.

In our previous comparative study of the photothermal efficiency of gold nanorods, silica/gold nanoshells, and Au–Ag nanocages,[33] the Au–Ag nanocages were shown to have the maximal specific photothermal efficiency per metal particle mass, followed by gold nanorods and silica/gold nanoshells. Here, we examined whether the composite nanoparticles retained their photothermal properties as compared to bare Au–Ag nanocages.

Figure 10a shows a general scheme for thermographic measurements. The water solutions of composite particles and bare nanocages (sample volume of 1.5 mL) were irradiated with an IR laser (808 nm, 1 W/cm$^2$, 5 min) from the top of Eppendorf tubes. The temperature–space distribution was recorded with a thermovision camera placed perpendicularly to the tube axis. For each irradiation run, the dynamic images from the thermovision camera were recorded every 10 s. The plots in Figure 10b illustrate the temperature kinetics recorded for the hottest region of the images. For suspensions with roughly equal number concentrations of about $2 \times 10^{14}$ L$^{-1}$, both particle types revealed close photothermal parameters. Specifically, the recorded temperature rapidly grows for 100 s and then slowly increases to steady-state values of about 75–80 °C. Note that the heating process is essentially nonlinear with respect to the particle concentration, as is evident from the temperature plots recorded after 4-fold dilution (curves 3 and 4).

The IR luminescence of nanocomposites (Figure 9) can be used for *in vivo* PDT experiments by some analogy with the data of Shirmanova *et al.*[51] from an *in vivo* study of photosensitizer pharmacokinetics as probed by fluorescence transillumination imaging. The promising capabilities of composite plasmonic-PDT nanostructures have been demonstrated quite recently by Jang *et al.*,[48] who developed a gold nanorod photosensitizer complex, (GNR)–Al(III) –AlPcS4, for noninvasive near-infrared fluorescence imaging and cancer therapy (AlPcS4 means phthalocyanine chloride tetrasulfonic acid). Here, we report preliminary data for *ex vivo* distribution of Au–Ag/$SiO_2$/Yb–HP nanocomposites in tumor-bearing mice. The biodistribution of pure Yb–HP molecules was also measured for direct comparison.

We used a xenografted mouse tumor model to assess the utility of the Au–Ag/$SiO_2$/Yb–HP composites for IR luminescence measurements with healthy and cancerous tissues. The nanocomposite solutions were introduced into the tail vein of mice ($n$ = 4) bearing Ehrlich carcinoma tumors. For comparison, free Yb–HP solution was intravenously administered to a similar mice group. At 20 h after injection, tumor, liver, spleen, muscle, and skin samples were taken for IR luminescence examination at an excitation wavelength of 405 nm. It follows from Figure 11 that the biodistributions of molecular Yb–HP and nanocomposites are similar with a good accumulation contrast in tumor tissue. In agreement with the published data for the biodistribution of gold nanoparticles,[52] we found significant accumulation of nanocomposites in the liver and spleen.

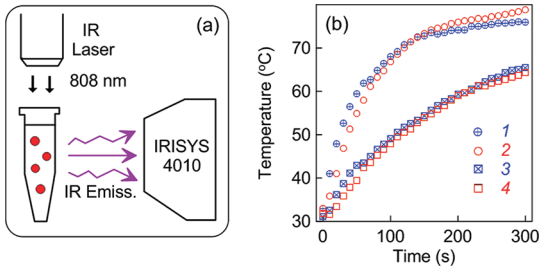


**Figure 10. Scheme for thermographic measurements (a) and the kinetics of heating for silica-coated Au–Ag nanocages (1, 3) and bare nanocages (2, 4). Measurements were made under NIR illumination (1 W/cm$^2$, 808 nm) of two suspensions with particle concentrations of $2 \times 10^{14}$ L$^{-1}$ (1, 2) and $0.5 \times 10^{14}$ L$^{-1}$ (3, 4).**

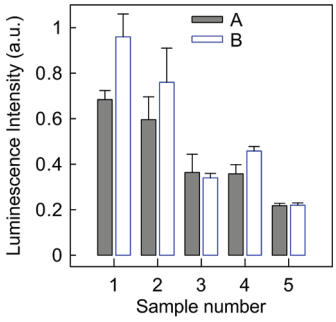


**Figure 11. The average integral luminescence intensities over the 900–1060-nm spectral band recorded with 405-nm excitation for five mice organs taken 20 h after intravenous injection of Yb–HP (A) and Au–Ag/$SiO_2$/(Yb–HP) nanocomposites (B). The numbers designate tumor (1), liver (2), spleen (3), muscle (4), and skin (5). Bars designate SD ($n$ = 4).**

It should be noted that the luminescence intensity of tissue samples can be affected by their intrinsic optical properties such as absorption, scattering, and autofluorescence. However, these factors are more important for UV–vis spectral band than for IR luminescence. For example, the autofluorescence of endogenous liver porphyrins can greatly contribute to the 630-nm fluorescence of exogenous porphyrin molecules but not to IR luminescence. Further, the IR (900–1050 nm) absorption coefficients of tissues are very low.[8] Accordingly, the data of Figure 11 should be considered an approximate yet reliable estimate of Yb–HP content. To make the IR-luminescence measurements more sample-independent, we developed a procedure for sample preparation and measurements (see Methods), in which the optical effects related to the intrinsic tissue properties are minimized by using homogenized tissue suspensions instead of intact samples. Our previous experiments showed that both methods (intact tissue samples and homogeneous suspensions) give comparable yet not identical results.[7]

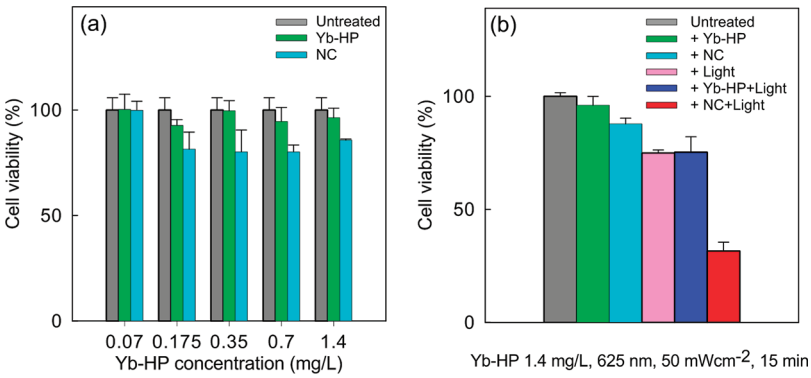


**Figure 12. (a) MTT assay for free Yb−HP and nanocomposites (NC) by using HeLa cells. The incubation time was 15 min and no light irradiation was applied. The abscissa labels indicate the concentrations of Yb−HP molecules in free Yb−HP solutions and in NC suspensions. (b) Cell viability as determined by MTT assay for HeLa cells under various treatment conditions. The concentrations of free Yb−HP and nanocomposites are 1.4 mg/L and 1.5 × $10^{13}$ particles/L, respectively; the light wavelength and power density are 625 nm and 50 mW $cm^{-2}$, respectively. Bars designate SD ($n$ = 3).**

For proving the potential utility of nanocomposites as a new theranostic agent, we examined the viability of HeLa cells (MTT assay, see Methods) at various concentrations of free Yb−HP and nanocomposites without light treatment. Additionally, an MTT cytotoxicity test was performed for HeLa cells incubated with free Yb−HP or nanocomposites. This was followed by 15-min light excitation at 625 nm and a power density of 50 mW $cm^{-2}$ (Figure 12).

It follows from Figure 12a that the viability of the cells after treatment with free Yb−HP molecules at concentrations ranging from 0.07 to 1.4 mg/L is close to that for the untreated control cells. Similar data were obtained for nanocomposites loaded with Yb−HP at the same concentrations, although the viability percentage was somewhat lower (80−100%). Irradiation of HeLa cells with a light-emitting diode (625 nm, 50 mW $cm^{-2}$, 15 min), with or without treatment with free Yb−HP molecules (1.4 mg/L), results in a similar decrease in cell viability to 75%. However, under the same irradiation conditions, we observed enhanced killing of HeLa cells incubated with nanocomposites loaded with the same concentration of Yb−HP (Figure 12b).

## CONCLUSIONS

In this work, nanocomposites with an Au−Ag nanocage core and a silica shell functionalized with the photosensitizer Yb−HP have been successfully fabricated. These novel nanocomposites have uniform distributions over the core and outer shell sizes, are stable in aqueous solution, and demonstrate an absorption peak near 400 nm, corresponding to the absorption of bound Yb−HP molecules. According to the spectral estimations, the number of Yb−HP molecules per one composite particle is about 4.8 × $10^4$. The visible fluorescence, IR-luminescence, and singlet oxygen generation of bound Yb−HP molecules are not quenched owing to metal−PS interaction because of the separation from the nanocage core by the mesoporous silica shell. Under UV excitation, the nanocomposites reveal quite intense fluorescent emission of light, which is visible by the naked eye because of two fluorescence peaks near 580 and 630 nm. To the best of our knowledge, the intense fluorescent peak at 580 nm of YB−HP complexes is reported here for the first time. Owing to the presence of an additional IR-luminescence band of Yb−HP molecules, the fabricated nanocomposites might one day be used for the *in vivo* optical monitoring and real-time therapy of tumors in combination with PDT and plasmonic heating. Furthermore, similarly to the silica-coated nanorods,[53] the silica-coated Au−Ag nanocages can possess one more useful modality related to efficient generation of optoacoustic response, which is now used widely in biomedical studies.[54]

In general, tissues have high molar extinction coefficients and small penetration depths at visible wavelengths.[8] Therefore, HP and Yb−HP are not optimal dyes for fluorescence and IR-luminescence bioimaging because of the 400-nm excitation wavelength. Perhaps it would be a good idea to functionalize composite particles with a luminescent dye possessing NIR excitation/emission bands. For example, we have recently fabricated antimicrobial nanocomposites containing silica/gold nanoshells or Au−Ag nanocages and indocyanine green (ICG).[55] ICG is the most red-shifted fluorescence dye (810-nm emission at 780-nm excitation) approved for clinical practice. Unfortunately, ICG has no PDT activity either. The same is true for other dyes approved for clinical applications (porphyrins, phthalocyanines, texafrins, bacteriochlorins), which are quite limited in number. Being effective PDT agents, these dyes have no IR-luminescence. Therefore, further studies are needed to find optimal theranostic hybrid particles possessing photothermal, photodynamic, and IR-luminescence bioimaging modalities.

## MATERIALS AND METHODS

**Materials.** The following reagents were used: $AgNO_3$ (>99.9%; Aldrich, 20.913-9), ethyleneglycol (EG) (99%, Aldrich; 293237), poly(vinyl pyrrolidone) (PVP) ($M_w$ = 55000; Sigma–Aldrich; 85.656-8), isopropyl alcohol (IPA) (chemical grade; Vekton Co., Russia), tetraethyl orthosilicate (TEOS) (98%; Aldrich), 30% aqueous solution of ammonia (Aldrich), 3-aminopropyltriethoxysilane (APTES) (98%; Sigma), acetone (chemical grade; Vekton, Russia), absolute ethanol (99.99%; Sharlau; 64-17-5), $Na_2S \times 9H_2O$ (analytical grade; GOST 2053-77; Radian Co., Russia), condensed argon (99.99%), 1-ethyl-3-(3-dimethylaminopropyl) carbodiimide (Sigma–Aldrich), dimethyl sulfoxide (DMSO), tetrachloroauric acid (>99%; Sigma–Aldrich), nitric acid (chemical grade; GOST 4461-77; Radian, Russia), hydrochloric acid (chemical grade; GOST 3118-77; Radian, Russia), Milli-Q water (18 MOhm × cm; Millipore), gum arabic (Sigma–Aldrich). Yb–2,4-dimethoxyhematoporphyrin IX dipotassium salt was obtained as described in ref 7. The chemical structures and physical data can be found in refs 7 and 56.

**Fabrication of Silver Nanocubes.** Au–Ag nanocages were prepared by a two-step process previously reported by Skrabalak *et al.*,[37] with a minor modification.[57] In the first step, Ag nanocube templates were prepared. Briefly, 30 mL of ethylene glycol was added to a 250-mL round-bottomed flask and was heated in an oil bath at 150 °C under magnetic stirring. After 50-min preheating, a flow of argon was introduced at a rate of 1200 mL/min. After 10 min, a sodium sulfide solution in EG (0.35 mL, 3 mM) was quickly injected into the preheated EG solution, followed by injection of a PVP solution in EG (7.5 mL, 20 g/L) and 8 min later by injection of a silver nitrate solution in EG (2.5 mL, 48 g/L). Shortly after the addition of $AgNO_3$, the reaction solution went through four distinct stages of color change from golden yellow to deep red, reddish gray, and then green ocher within about 30 min. The reaction solution was then quenched by placing the reaction flask in an ice–water bath. The resultant product was washed by centrifugation (12000*g*, 30 min) and was redispersed with acetone, followed by redispersion in ethanol to remove excess EG and PVP. Finally, the Ag nanocubes were redispersed in 40 mL of ethanol. In a typical synthesis, the product contained 0.05 g of solid Ag, corresponding to cubic nanoparticles with an edge length of about 40 ± 5 nm, a number concentration of about $1.7 \times 10^{15}$ $L^{-1}$, and an extinction coefficient at 440 nm of about 220 $cm^{-1}$.

**Fabrication of Au–Ag Nanocages.** The isolated Ag nanocubes were converted into Au nanocages *via* the galvanic replacement reaction.[37] Briefly, a PVP water solution (100 mL, 1 g/L) was heated at 100 °C under magnetic stirring, followed by injection of 2 mL of the as-prepared nanocubes suspension in ethanol. After 3 min, 10 mL of a 1 mM $HAuCl_4$ solution was added drop by drop over 10 min. The addition of $HAuCl_4$ to the reaction mixture was accompanied by four distinct changes in color from orange yellow to deep red, purple, and finally light blue. The appearance of a light blue color indicates the successful formation of Au nanocages owing to the galvanic replacement reaction between solid Ag and $Au^{3+}$ ions. The reaction solution was then quenched by placing the reaction flask in an ice–water bath. This was followed by the addition of $NH_4OH$ (0.7 mL, 30 wt %) to dissolve solid AgCl formed as a byproduct. The nanocages were washed by centrifugation (12000*g*, 20 min) and were redispersed with water three times. Finally, the Au nanocages were redispersed in 4 mL of water. In a typical synthesis, the product contained nanocages with an average edge length of about (43–46) ± 5 nm and the plasmon resonance peak near 750–800 nm, depending on the Ag/Au conversion ratio.

**Fabrication of Silica-Coated Nanocages.** In a typical silica-coating procedure, 4 mL of as-prepared Au nanocages was added to 18 mL of isopropyl alcohol. Under continuous magnetic stirring, a water–ammonia solution (0.5 mL, 30 wt %) and TEOS (0.05 mL) were consecutively added to the reaction mixture in order to obtain Au–Ag nanocages with a 45-nm silica-shell coating (Au–Ag/$SiO_2$). The reaction was allowed to proceed for 50 min at room temperature under continuous stirring. The resulting Au–Ag/$SiO_2$ colloids were purified by repeated centrifugation at 6000*g* for 10 min and by washing with ethanol in order to remove reaction impurities. In between the different centrifugation steps, the samples were ultrasonically redispersed. Finally, the colloids were redispersed in 10 mL of ethanol.

**Fabrication of Au–Ag/$SiO_2$/Yb–HP Nanocomposites.** First, the silica-coated nanocages were functionalized with amine groups. A 50 μL portion of APTES was added to 10 mL of silica-coated nanocages suspension. The reaction was allowed to proceed for 1 h at 70 °C without stirring. The amino functionalization reaction could be monitored visually by observing the separation of the solution into two layers as the amino-coated nanoparticles precipitated to the bottom, leaving a clear ethanol solution at the top. The precipitate was washed several times with water and was finally redispersed ultrasonically in 10 mL of a Yb–HP water solution (200 mg/L). Because of the electrostatic interaction between the positively charged primary amine groups on the nanoparticle surface and the carboxyl groups of Yb–HP, the photosensitizer was adsorbed on the silica-coated nanocages. To obtain strong covalent binding, we used EDC as a zero-length cross-linking agent to couple amino and carboxyl groups. A 1 mL portion of EDC solution in DMSO (1 g/L) was added to the suspension under continuous stirring. The reaction was allowed to proceed for 2 h at room temperature. Composite Au–Ag/$SiO_2$/Yb–HP nanoparticles were washed several times by centrifugation (6000*g*, 10 min) and reinsertion in 10 mL of water. For enhancing colloidal stability, a gum arabic solution (100 μL, 2 g/L) was added to the composite suspension (10 mL). After 10 min, the nanocomposites were washed one more time and were finally redispersed in 10 mL of water. The final product contained silica-coated nanocages with an edge length of about (43–46) ± 5 nm, silica shell thickness of about 45 nm, a number concentration of about $2 \times 10^{11}$ $mL^{-1}$, and a Yb–HP concentration of about 10 g/L or about 48000 Yb–HP molecules per nanoparticle.

**Measurements.** TEM images were obtained with a Libra-120 transmission electron microscope (Carl Zeiss, Germany). Extinction spectra were recorded with a Specord BS-250 UV–vis spectrophotometer (Analytik Jena, Germany). DLS measurements were made with a Zetasizer Nano-ZS instrument (Malvern, UK).

The gold and silver percentages in Au–Ag nanocages were determined by atomic absorption spectroscopy. In a typical protocol, 50 μL of Au–Ag nanocages solution was added to 950 μL of aqua regia (3HCl/1$HNO_3$). After 1 h, 9 mL of water was added to the reaction mixture. Au and Ag contents were determined with a Dual Atomizer Zeeman AA spectrometer iCE 3500 (Thermo Scientific Inc., USA). To calibrate the atomic absorption spectrometer (AAS) for quantitative analysis of Au and Ag, we used two procedures. In the first one, the AAS was calibrated by using an $HAuCl_4$ solution in 0.1 M HCl and an aqueous solution of $AgNO_3$. In the second method, we used gold (15 nm) and silver (20 nm) colloids with known Au and Ag contents, as determined from citrate reduction of $HAuCl_4$ and EDTA reduction of $AgNO_3$.[58] These colloids were treated by adding the same aqua regia (3HCl/1$HNO_3$) mixture as used for Au–Ag nanocages. Both calibration procedures gave consistent data within 10% experimental error.

For measurements of visible fluorescence spectra, we used a Perkin-Elmer LS-55 spectrofluorometer. The IR-luminescence spectra of Yb–HP were measured with a homemade setup (Institute of Radio Engineering and Electronics, Russian Academy of Sciences) that includes high-power super luminescent diodes (400 nm, 50 mW and 530 nm, 70 mW) and an FSD-8 minispectrometer operating in the spectral interval 250–1100 nm.

**Testing the Integrity of Nanocomposites.** To test nanocomposite integrity to pH variations, washing, or leaching of the dye molecules, we placed 500 μL of particle solutions in three tubes and adjusted their pH to 2, 7, and 13 by adding 20 μL of 1 M HCl, 100 mM PBS, and 1 M NaOH, respectively. After 10 min following the pH adjustment, all samples were centrifuged and redispersed in solutions containing 500 μL of water and 20 μL of the same pH-adjusting supplements (1 M HCl, 100 mM PBS, and 1 M NaOH). Finally, the UV–vis spectra of the samples were measured. The same test was also performed for a longer incubation time (10 h).

**Determination of Yb−HP in Nanocomposite Particles.** Composite nanoparticles were centrifuged and redispersed in a washing mixture consisting of ethanol (45%, v/v), dimethyl sulfoxide (DMSO, 45%), and water (10%). The redispersed particles were treated with ultrasound for 10 min and then were centrifuged and redispersed in water. The washing-mixture supernatant liquid and redispersed particles were used for measurements of UV−vis spectra.

**Detection of Singlet Oxygen Generation.** The time-dependent consumption of oxygen in PS-containing blood samples was measured as described in detail in ref 59. Briefly, the oxygenation degree of the samples was determined from transmittance spectra (510−580 nm) measured with a 125-$\mu$m layer containing 33% (v/v) of red blood cells, 50% of blood serum, and 17% of a PS aqueous solution. The kinetics of oxygen saturation were measured by using the time-dependent spectra of light from a halogen lamp source, diffusely transmitted through samples that were continuously irradiated by 6-s laser light pulses (633 nm, 30 mW/cm$^2$) followed by 10-s dark pauses. These spectra were measured with a LESA-01-Biospec (Russia) setup[59] that allows real-time measurements of the diffuse transmittance spectra (430−630 nm), the backscattered laser radiation (633 or 680 nm), and PS fluorescence spectra (690−850 nm). The number of the singlet oxygen molecules produced by one PS molecule at an irradiation dose of 1 J/cm$^2$ was calculated by eq 4.

**Photothermal Measurements.** For time-dependent photothermal measurements, we used a homemade setup (Figure 10) consisting of an IR laser (ACCULASER, 808 nm, 1 W at the distal fiber end, CW regime). The samples were placed in Eppendorf tubes and were irradiated from the top of the tubes (5 min, laser power density of 2.5 W/cm$^2$ at a beam diameter of 6 mm). For real-time measurements of spatial temperature distribution in both *in vivo* and *in vitro* experiments, an IR Imager IRISYS 4010 (Infrared Integrated System Limited, UK) was used.

**Biodistribution Measurements.** Animals were bred under SPF (Standard of Care for Specific Pathogen Free Animals) conditions and were barrier-maintained during the experiment. Drinking water and conventional food were provided *ad libitum*. The experimental protocol was approved by an independent ethic committee prior to the study. Ehrlich carcinoma cells were subcutaneously implanted into the hind flank of each mouse, and tumors were allowed to grow for about two weeks. Animals were divided in two equivalent groups (four mice per group). The nanocomposite and free Yb−HP solutions were introduced into the tail vein of the mice from the first and second group, respectively. At 20 h after injection, the following organs were collected for IR-luminescence examination: tumor, liver, spleen, muscle, and skin. For *ex vivo* measurements of IR luminescence, we used a prototype of the fiber-laser oncofluorimeter,[7] recording the integral backscattered luminescence signal within the 900−1060 nm spectral interval at a 405-nm excitation (20 mW at the distal fiber end) of samples placed in the wells of a culturing plate. The excitation and recording directions were close to the plate normal. The biodistribution of nanocomposites or free Yb−HP can be estimated in terms of the average integral IR-luminescence intensity (the area $S$ under the IR-luminescence spectrum) or in terms of the luminescence contrast, calculated as the ratio $S/S_0$, where $S_0$ is the area under the IR-luminescence spectra of a healthy reference tissue. In this work, the reported data correspond to the average integral intensities.

We also developed a procedure for sample preparation and measurements, in which 100 mg of tissues was homogenized in 4 mL of PBS in a hand glass homogenizer to a homogeneous mass. The resulting suspension was diluted with PBS to a mass/volume concentration of 25 g/L and was placed in a standard four-side 1-cm cell for fluorescence measurements. UV−vis fluorescence and IR-luminescence spectra (300−1050 nm, observation angle of 90°) were measured with a homemade setup (IREE RAS) at 400-nm or 530-nm excitation by high-power superluminescent diodes (50 mW and 70 mW, respectively).

**Cell Viability Determination.** HeLa cells (Saratov Science Research Veterinary Station, Saratov, Russia) were maintained at 37 °C and 5% $CO_2$ in complete DMEM medium (Biolot Co., Russia) supplemented with 10% bovine serum, 300 mg/L L-glutamine, 100 mg/L ampicillin, 50 mg/L gentamicin, and 2.5 mg/L amphotericin B (all from Biolot). The cell suspension was centrifuged at 1000*g* for 5 min and then was redispersed in Hanks' solution (Biolot). A 1 mL portion of the cell suspension ($10^8$ cells/L) was incubated with 0.2 mL of free Yb−HP or nanocomposite solutions for 15 min, and then the mixture was illuminated with a light-emitting diode (AFS phototherapeutic apparatus, Polyronic Co., Russia) for 15 min at 625 nm and a power density of 50 mW cm$^{-2}$. Untreated HeLa cells and HeLa cells treated separately with PS (Yb−HP and NC−$SiO_2$−Yb−HP) or light were used as controls. Cell viability was measured by the MTT assay.[60] In brief, after incubation with PSs followed by light illumination, the cells were centrifuged at 1000*g* for 5 min, redispersed in 0.5 mL MTT solution (Sigma, USA), and incubated for 1 h in the dark at 37 °C. Then, the cells were centrifuged at 1000*g* for 5 min and redispersed in 0.5 mL DMSO (ACS grade DMSO, Amresco, USA) to dissolve formazan crystals. The samples were centrifuged at 12000*g* for 5 min in 1.5 mL Eppendorf tubes (Eppendorf Minispin), and 0.2 mL of the supernatant liquids was transferred to 96-well plates. Absorbance values at 492 nm were collected on a Multiskan Ascent microplate reader (Thermo Fisher Scientific Inc.).

*Acknowledgment.* This research was supported by grants from the Russian Foundation for Basic Research and from the President and the Ministry of Education and Science of the Russian Federation. We thank K. Shchamkhalov for IR-luminescence measurements, S. Staroverov for his help with the MTT assay, and D.N. Tychinin (IBPPM RAS) for his help in preparation of the manuscript.

*Supporting Information Available:* The Supporting Information file contains TEM images and statistical data for Ag cubes, Au−Ag nanocages, and Au−Ag/SiO2/Yb−HP nanocomposites; calibration plots for determination Yb-HP concentration in water and ethanol−DMSO−water mixture; data on stability of nanocomposites at pH 2, 7, and 13; and the concentration dependences of fluorescence spectra and their corrections to the absorption of excited and emitted light. This material is available free of charge *via* the Internet at http://pubs.acs.org.

## REFERENCES AND NOTES

1. Triesscheijn, M.; Baas, P.; Schellens, J. H.; Stewart, F. A. Photodynamic Therapy in Oncology. *Oncologist* **2006**, *11*, 1034–1044.
2. Olivo, M.; Bhuvaneswari, R.; Lucky, S. S.; Dendukuri, N.; Thong, P. S.-P. Targeted Therapy of Cancer Using Photodynamic Therapy in Combination with Multifaceted Antitumor Modalities. *Pharmaceuticals* **2010**, *3*, 1507–1529.
3. Wilson, B. C. Photodynamic Therapy/Diagnostics. In: *Handbook of Photonics for Biomedical Science*; Tuchin, V. V., Ed.; CRC Press: Boca Raton, 2010; pp 650−686.
4. Chatterjee, D. K.; Li, S. F.; Zhang, Y. Nanoparticles in Photodynamic Therapy: An Emerging Paradigm. *Nanotechnology* **2008**, *60*, 1627–1637.
5. Loschenov, V. B.; Konov, V. I.; Prokhorov, A. M. Photodynamic Therapy and Fluorescence Diagnostics. *Laser Phys.* **2000**, *10*, 1188–1207.
6. Diamond, K. R.; Farrell, T. J.; Patterson, M. S. Measurement of Fluorophore Concentrations and Fluorescence Quantum Yield in Tissue-Simulating Phantoms Using Three Diffusion Models of Steady-State Spatially Resolved Fluorescence. *Phys. Med. Biol.* **2003**, *48*, 4135–4149.
7. Ivanov, A. V.; Rumyantseva, V. D.; Shchamkhalov, K. S.; Shilov, I. P. Luminescence Diagnostics of Malignant Tumors in the IR Spectral Range Using Yb−Porphyrin Metallocomplexes. *Laser Phys.* **2010**, *20*, 2056–2065.
8. Tuchin, V. V. *Tissue Optics: Light Scattering Methods and Instrumentation for Medical Diagnostics*, 2nd ed.; SPIE Press: Bellingham, WA, 2008.
9. Konan, Y. N.; Gurny, R.; Allemann, E. State of the Art in the Delivery of Photosensitizers for Photodynamic Therapy. *J. Photochem. Photobiol. B* **2002**, *66*, 89–106.

10. Bechet, D.; Couleaud, P.; Frochot, C.; Viriot, M.-L.; Guillemin, F.; Barberi-Heyob, M. Nanoparticles as Vehicles for Delivery of Photodynamic Therapy Agents. *Trends Biotechnol.* **2008**, *26*, 612–621.
11. Juzenas, P.; Chen, W.; Sun, Y.-P.; Coelho, M. A. N.; Generalov, R.; Generalova, N.; Lie, I. C. Quantum Dots and Nanoparticles for Photodynamic and Radiation Therapies of Cancer. *Adv. Drug Delivery Rev.* **2008**, *60*, 1600–1614.
12. Gong, X.; Milic, T.; Xu, C.; Batteas, J. D.; Drain, C. M. Preparation and Characterization of Porphyrin Nanoparticles. *J. Am. Chem. Soc.* **2002**, *124*, 14290–14291.
13. Chen, W.; Zhang, J. Using Nanoparticles to Enable Simultaneous Radiation and Photodynamic Therapies for Cancer Treatment. *J. Nanosci. Nanotechnol.* **2006**, *6*, 1159–1166.
14. Chen, B.; Pogue, B. W.; Hasan, T. Liposomal Delivery of Photosensitising Agents. *Expert Opin. Drug Delivery* **2005**, *2*, 477–487.
15. Tsai, T.; Yang, Y.-T.; Wang, T.-H.; Chien, H.-F.; Chen, C.-T. Improved Photodynamic Inactivation of Gram-Positive Bacteria Using Hematoporphyrin Encapsulated in Liposomes and Micelles. *Lasers Surg. Med.* **2009**, *41*, 316–322.
16. Leung, S. J.; Kachur, X. M.; Bobnick, M. C.; Romanowski, M. Wavelength-Selective Light-Induced Release from Plasmon Resonant Liposomes. *Adv. Funct. Mater.* **2011**, *21*, 1113–1121.
17. Cheng, S.-H.; Lee, C.-H.; Yang, C.-S.; Tseng, F.-G.; Mou, C.-Y.; Lo, L.-W. Mesoporous Silica Nanoparticles Functionalized with an Oxygen-Sensing Probe for Cell Photodynamic Therapy: Potential Cancer Theranostics. *J. Mater. Chem.* **2009**, *19*, 1252–1257.
18. Li, L.-L.; Fu, X.-F.; Ren, Z.; Zhao, Y.-G.; Feng, W.; Yan, C.-H. Hierarchical Self-Assembly of Superlattice Hybrids Consisting of Periodic and Alternating Cores of Porphyrin Molecules Separated by Nanoscale Silica Walls. *Langmuir* **2010**, *26*, 15730–15733.
19. Zhang, R.; Wu, C.; Tong, L.; Tang, B.; Xu, Q.-H. Multifunctional Core-Shell Nanoparticles as Highly Efficient Imaging and Photosensitizing Agents. *Langmuir* **2009**, *25*, 10153–10158.
20. Cheng, S.-H.; Lee, C.-H.; Chen, M.-C.; Souris, J. S.; Tseng, F.-G.; Yang, C.-S.; Mou, C.-Y.; Chen, C.-T.; Lo, L.-W. Tri-functionalization of Mesoporous Silica Nanoparticles for Comprehensive Cancer Theranostics — the Trio of Imaging, Targeting and Therapy. *J. Mater. Chem.* **2010**, *20*, 6149–6157.
21. Bardhan, R.; Chen, W.; Bartels, M.; Perez-Torres, C.; Botero, M. F.; McAninch, R. W.; Contreras, A.; Schiff, R.; Pautler, R. G.; Halas, N. J.; et al. Tracking of Multimodal Therapeutic Nanocomplexes Targeting Breast Cancer *in Vivo*. *Nano Lett.* **2010**, *10*, 4920–4928.
22. Khlebtsov, N. G.; Dykman, L. A. Optical Properties and Biomedical Applications of Plasmonic Nanoparticles. *J. Quant. Spectr. Radiat. Transfer* **2010**, *111*, 1–35.
23. Zhang, L.; Li, X.; Mu, J. Self-Assembly of Porphyrin-Based Supramolecules and their Characteristics on Gold Nanoparticles. *Coll. Surf. A* **2007**, *302*, 219–224.
24. Ohyama, J.; Hitomi, Y.; Higuchi, Y.; Shinagawa, M.; Mukai, H.; Kodera, M; Teramura, K.; Shishido, T.; Tanaka, T. One-Phase Synthesis of Small Gold Nanoparticles Coated by a Horizontal Porphyrin Monolayer. *Chem. Commun.* **2008**, 6300–6302.
25. Kanehara, M.; Takahashi, H.; Teranishi, T. Gold (0) Porphyrins on Gold Nanoparticles. *Angew. Chem., Int. Ed.* **2008**, *47*, 307–310.
26. Reum, N.; Fink-Straube, C.; Klein, T.; Hartmann, R. W.; Lehr, C.-M.; Schneider, M. Multilayer Coating of Gold Nanoparticles with Drug-Polymer Coadsorbates. *Langmuir* **2010**, *26*, 16901–16908.
27. Kotiaho, A.; Lahtinen, R.; Efimov, A.; Lehtivuori, H.; Tkachenko, N. V.; Kanerva, T.; Lemmetyinen, H. Synthesis and Time-Resolved Fluorescence Study of Porphyrin-Functionalized Gold Nanoparticles. *J. Photochem. Photobiol., A* **2010**, *212*, 129–134.
28. Sicard, C.; Brayner, R.; Margueritat, J.; Hémadi, M.; Couté, A.; Yéprémian, C.; Djediat, C.; Aubard, J.; Fiévet, F.; Livage, J.; *et al.* Nano-Gold Biosynthesis by Silica-Encapsulated Micro-Algae: A ``Living'' Bio-Hybrid Material. *J. Mater. Chem.* **2010**, *20*, 9342–9347.
29. Hone, D. C.; Walker, P. I.; Evans-Gowing, R.; FitzGerald, S.; Beeby, A.; Chambrier, I.; Cook, M. J.; Russell, D. A. Generation of Cytotoxic Singlet Oxygen *via* Phthalocyanine-Stabilized Gold Nanoparticles: A Potential Delivery Vehicle for Photodynamic Therapy. *Langmuir* **2002**, *18*, 2985–2987.
30. Wieder, M. E.; Hone, D. C.; Cook, M. J.; Handsley, M. M.; Gavrilovic, J.; Russell, D. A. Intracellular Photodynamic Therapy with Photosensitizer-Nanoparticle Conjugates: Cancer Therapy Using a "Trojan Horse". *Photochem. Photobiol. Sci.* **2006**, *5*, 727–734.
31. Zhao, T.; Wu, H.; Yao, S. Q.; Xu, Q.-H.; Xu, G. Q. Nanocomposites Containing Gold Nanorods and Porphyrin-Doped Mesoporous Silica with Dual Capability of Two-Photon Imaging and Photosensitization. *Langmuir* **2010**, *26*, 14937–14942.
32. Cobley, C. M.; Chen, J.; Cho, E. C.; Wang, L. V.; Xia, Y. Gold Nanostructures: A Class of Multifunctional Materials for Biomedical Applications. *Chem. Soc. Rev.* **2011**, *40*, 44–56.
33. Khlebtsov, B. N.; Khanadeev, V. A.; Maksimova, I. L.; Terentyuk, G. S.; Khlebtsov, N. G. Silver Nanocubes and Gold Nanocages: Fabrication and Optical and Photothermal Properties. *Nanotechnol. Russ.* **2010**, *5*, 454–468.
34. Ratto, F.; Matteini, P.; Centi, S.; Rossi, F.; Fusi, F.; Pini, R. Fabrication and Optical Stability of Silanized Gold Nanorods as Multifunctional Transducers of Near Infrared Light. *Proc. SPIE* **2011**, *7910*, 79101E.
35. Zhu, C.-L.; Lu, C.-H.; Song, X.-Y.; Yang, H.-H.; Wang, X.-R. Bioresponsive Controlled Release Using Mesoporous Silica Nanoparticles Capped with Aptamer-Based Molecular Gate. *J. Am. Chem. Soc.* **2011**, *133*, 1278–1281.
36. Gouterman, M.; Schumaker, C. D.; Srivastava, T. S.; Yonetani, T. Absorption and Luminescence of Yttrium and Lanthanide Octaethylporphin Complexes. *Chem. Phys. Lett.* **1976**, *40*, 456–461.
37. Skrabalak, S. E.; Au, L.; Li, X.; Xia, Y. Facile Synthesis of Ag Nanocubes and Au Nanocages. *Nat. Protoc.* **2007**, *2*, 2182–2190.
38. Panfilova, E. V.; Khlebtsov, B. N.; Burov, A. M.; Khlebtsov, N. G. A Study of the Polyol Process Parameters Controlling High Yield of Silver Nanocubes. *Colloid J.* **2011**, in press.
39. Sun, Y.; Xia, Y. Mechanistic Study on the Replacement Reaction between Silver Nanostructures and Chloroauric Acid in Aqueous Medium. *J. Am. Chem. Soc.* **2004**, *126*, 3892–3901.
40. Stöber, W.; Fink, A.; Bohn, J. Controlled Growth of Monodisperse Silica Spheres in the Micron Size Range. *J. Colloid Interface Sci.* **1968**, *26*, 62–69.
41. Khlebtsov, B. N.; Khlebtsov, N. G. Enhanced Solid-Phase Immunoassay Using Gold Nanoshells: Effect of Nanoparticle Optical Properties. *Nanotechnology* **2008**, *19*, 435703.
42. Joo, S. H.; Park, J. Y.; Tsung, C.-K.; Yamada, Y.; Yang, P.; Somorjai, G. A. Thermally Stable Pt/Mesoporous Silica Core–Shell Nanocatalysts for High-Temperature Reactions. *Nat. Mater.* **2009**, *8*, 126–131.
43. Cho, E. C.; Kim, C.; Zhou, F.; Cobley, C. M.; Song, K. H.; Chen, J.; Li, Z.-Y.; Wang, L. V.; Xia, Y. Measuring the Optical Absorption Cross Sections of Au–Ag Nanocages and Au Nanorods by Photoacoustic Imaging. *J. Phys. Chem. C* **2009**, *113*, 9023–9028.
44. Bohren, C. F.; Huffman, D. R. *Absorption and Scattering of Light by Small Particles*; John Wiley&Sons: New York, 1983.
45. Lakowicz, J. R.; Ray, K.; Chowdhury, M.; Szmacinski, H.; Fu, Y.; Zhang, J.; Nowaczyk, K. Plasmon-Controlled Fluorescence: A New Paradigm in Fluorescence Spectroscopy. *Analyst* **2008**, *133*, 1308–1346.
46. Lakowicz, J. R. *Principles of Fluorescence Spectroscopy*, 3rd ed.; Springer: New York, 2006.
47. Stratonnikov, A. A.; Douplik, A. Yu.; Loschenov, V. B. Oxygen Consumption and Photobleaching in Whole Blood Incubated with Photosensitizer Induced by Laser Irradiation. *Laser Phys.* **2003**, *13*, 1–21.

48. Jang, B.; Park, J.-Y.; Tung, C.-H.; Kim, I.-H.; Choi, Y. Gold Nanorod-Photosensitizer Complex for Near-Infrared Fluorescence Imaging and Photodynamic/Photothermal Therapy *In Vivo*. *ACS Nano* **2011**, *5*, 1086–1094.
49. Kennedy, L. C.; Bickford, L. R.; Lewinski, N. A.; Coughlin, A. J.; Hu, Y.; Day, E. S.; West, J. L.; Drezek, R. A. A New Era for Cancer Treatment: Gold-Nanoparticle-Mediated Thermal Therapies. *Small* **2011**, *7*, 169–183.
50. Kuo, T. R.; Hovhannisyan, V. A.; Chao, Y. C.; Chao, S. L.; Chiang, S. J.; Lin, S. J.; Dong, C. Y.; Chen, C. C. Multiple Release Kinetics of Targeted Drug from Gold Nanorod Embedded Polyelectrolyte Conjugates Induced by Near-Infrared Laser Irradiation. *J. Am. Chem. Soc.* **2010**, *132*, 14163–14171.
51. Shirmanova, M.; Zagaynova, E.; Sirotkina, M.; Snopova, L.; Balalaeva, I.; Krutova, I.; Lekanova, N.; Turchin, I.; Orlova, A.; Kleshnin, M. *In Vivo* Study of Photosensitizer Pharmacokinetics by Fluorescence Transillumination Imaging. *J. Biomed. Opt.* **2010**, *15*, 048004.
52. Khlebtsov, N.; Dykman, L. Biodistribution and Toxicity of Engineered Gold Nanoparticles: A Review of *in Vitro* and *in Vivo* Studies. *Chem. Soc. Rev.* **2010**, *40*, 1647–1671.
53. Chen, Y.-S.; Frey, W.; Kim, S.; Kruizinga, P.; Homan, K.; Emelianov, S. S. Silica-Coated Gold Nanorods as Photoacoustic Signal Nanoamplifiers. *Nano Lett.* **2011**, *11*, 348–354.
54. Li, C.; Wang, L. V. Photoacoustic Tomography and Sensing in Biomedicine. *Phys. Med. Biol.* **2009**, *54*, R59–R97.
55. Tuchina, E. S.; Tuchin, V. V.; Khlebtsov, B. N.; Khlebtsov, N. G. Phototoxic Effect of Conjugates of Plasmon-Resonance Nanoparticles with Indocyanine Green Dye on *Staphylococcus Aureus* Induced by IR Laser Radiation. *Quant. Electron.* **2011**, *41*, 354–359.
56. Rumyantseva, V. D.; Mironov, A. F.; Shilov, I. P.; Shchamkhalov, K. S.; Ivanov, A. V.; Baryshnikov, A. Yu. Russian Federation Patent No. 2411243, 2011.
57. Zhang, Q.; Cobley, C. M.; Au, L.; McKiernan, M.; Schwartz, A.; Chen, J.; Wen, L.; Xia, Y. Production of Ag Nanocubes on a Scale of 0.1 g per Batch by Protecting the NaHS-Mediated Polyol Synthesis with Argon. *ACS Appl. Mater. Interfaces* **2009**, *1*, 2044–2048.
58. Khlebtsov, N. G.; Dykman, L. A.; Krasnov, Ya. M.; Mel'nikov, A. G. Light Absorption by the Clusters of Colloidal Gold and Silver Particles Formed During Slow and Fast Aggregation. *Colloid J.* **2000**, *62*, 765–779.
59. Ryabova, A. V.; Stratonnikov, A. A.; Loshchenov, V. B. Laser Spectroscopy Technique for Estimating the Efficiency of Photosensitizers in Biological Media. *Quantum Electron.* **2006**, *36*, 562–568.
60. Oez, S; Platzer, E.; Welte, K. A Quantitative Colorimetric Method to Evaluate the Functional State of Human Polymorphonuclear Leukocytes. *Blut* **1990**, *60*, 97–102.